

Lawrence Berkeley National Laboratory

LBL Publications

Title

Multiwell Fiber Optic Sensing Reveals Effects of CO2 Flow on Triggered Seismicity

Permalink

<https://escholarship.org/uc/item/0w7458xr>

Journal

Seismological Research Letters, 94(5)

ISSN

0895-0695

Authors

Glubokovskikh, Stanislav

Shashkin, Pavel

Shapiro, Serge

et al.

Publication Date

2023-09-01

DOI

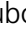



10.1785/0220230025

Copyright Information

This work is made available under the terms of a Creative Commons Attribution-NonCommercial-ShareAlike License, available at <https://creativecommons.org/licenses/by-nc-sa/4.0/>

Peer reviewed

Multiwell Fiber Optic Sensing Reveals Effects of CO₂ Flow on Triggered Seismicity

Stanislav Glubokovskikh¹, Pavel Shashkin², Serge Shapiro³, Boris Gurevich², and Roman Pevzner²

Abstract




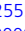

Induced seismicity is one of the main risks for gigaton-scale geological storage of carbon dioxide (CO₂). Thus, passive seismic monitoring is often recommended as a necessary component of the monitoring systems for CO₂ storage projects, with a particular focus on risk mitigation. We present the first field study, CO2CRC Otway Project Stage 3 (Victoria, Australia), where distributed acoustic sensing (DAS) enabled high-precision tracking of the induced seismicity triggered by a small CO₂ injection and also informed the reservoir models. In 610 days of passive seismic monitoring of the Stage 3 injection, we detected 17 microseismic events (maximum moment magnitude M_w 0.1) using five deep boreholes equipped with enhanced-sensitivity optical fiber. The DAS array has sensitivity sufficient for detection and location of induced events with $M_w \sim -2$ in a monitoring borehole located up to 1500 m away. Thanks to the dense spatial sampling by the DAS, we were able to estimate the focal mechanisms for events with $M_w > -1.5$; although the monitoring boreholes provided very limited angular coverage. The main cluster of the events has the same location and source mechanism as the one triggered by the previous CO₂ injection at the Otway Project site, Stage 2C. Surprisingly, the Stage 2C and Stage 3 events closely followed the actual movement of the CO₂ saturation plume front (not the pressure front), as observed using controlled-source reflection seismic images. The nature of the plume-fault interaction remains unclear, but some alteration of the fault gouge by CO₂ might be responsible for the faults' reactivation by the pressure perturbation. Importantly, the seismogenic fault could not be identified in the seismic images and was only revealed by DAS observations, which also demonstrated the signature of fluid–rock interaction, that may control the CO₂ flow.

Cite this article as Glubokovskikh, S., P. Shashkin, S. Shapiro, B. Gurevich, and R. Pevzner (2023). Multiwell Fiber Optic Sensing Reveals Effects of CO₂ Flow on Triggered Seismicity, *Seismol. Res. Lett.* **XX**, 1–16, doi: [10.1785/0220230025](https://doi.org/10.1785/0220230025).

Introduction

Subsurface stress changes and complex thermal, mechanical, and chemical effects induced by geological carbon storage (GCS) may reactivate subsurface faults and lead to felt earthquakes (Vilarrasa *et al.*, 2019), CO₂ leakage pathways (White *et al.*, 2014), and even surface deformations (Vasco *et al.*, 2010). Therefore, induced seismicity monitoring is essential for the fluid injections at GCS projects. Yet only a few CO₂ injections dedicated to storage in saline aquifers have documented some triggered events: In Salah, Algeria (Goertz-Allmann *et al.*, 2014), two injections at the Decatur carbon capture and storage (CCS) site (United States) (Williams-Stroud *et al.*, 2020), Quest CCS Project (Canada) (Harvey *et al.*, 2021), Gorgon Project (Australia) (Chevron, 2021), and CO2CRC Otway Project Stage 2C (Australia) (Glubokovskikh *et al.*, 2022), with the largest seismic moment magnitude M_w 2.3 detected at the Gorgon Project.

Such scarcity of the documented induced seismicity is related to the fact that site operators tend to favor moderate injection pressure to reduce the risk of seismicity and associated public concerns. Yet, the need to increase global storage amounts to tens of gigatons is likely to require GCS projects to implement more aggressive injections (International Energy Agency [IEA], 2022), and thus monitoring of induced seismicity will become a critical matter. Distributed acoustic sensing (DAS) systems have great potential to become such a monitoring tool. Downhole-deployed DAS provides relatively inexpensive receiver array that

1. Lawrence Berkeley National Laboratory, Berkeley, California, U.S.A.,  <https://orcid.org/0000-0001-8815-8918> (SG); 2. Curtin University, Perth, Australia,  <https://orcid.org/0000-0003-1484-6405> (PS);  <https://orcid.org/0000-0002-2752-3528> (BG);  <https://orcid.org/0000-0002-2555-6860> (RP); 3. Freie Universität Berlin, Berlin, Germany,  <https://orcid.org/0000-0002-5062-2698> (SS)

*Corresponding author: sglubokovskikh@lbl.gov

© Seismological Society of America

is sensitive to the microearthquakes in a wide frequency range, as is evident from applications to enhanced geothermal systems (Lellouch *et al.*, 2020) or stimulation of unconventional reservoirs (Luo *et al.*, 2021; Staněk *et al.*, 2022). A 15,000 tonnes CO₂ injection during the Stage 3 CO₂CRC Otway Project in the Australian state of Victoria (Jenkins *et al.*, 2017) (referred to simply as Stage 3 subsequently) presented a unique opportunity to quantitatively characterize the seismicity triggered by two successive CO₂ injections using five deep boreholes instrumented with enhanced DAS systems (Pevzner *et al.* 2021).

Prior to Stage 3, a similar 15,000 tonnes injection into the same formation during the Stage 2C Otway Project also produced detectable induced seismicity as recorded by a dense array of vertical geophones buried 4 m below the surface (Pevzner, Urosevic, *et al.*, 2020). This array was not ideal for microseismic detection: At a depth of 4 m there is strong ambient noise, ocean-generated surface and body waves and active farming activity on the surface, resulting in relatively low signal-to-noise ratio (SNR). Furthermore, single-component measurements precluded polarization analysis and wave modes separation, whereas angular coverage of the array was insufficient for accurate estimation of the geometry and slip of the reactivated faults (Glubokovskikh *et al.*, 2022). Nevertheless, the microseismic monitoring along with time-lapse seismic images of the CO₂ plume suggested that the events were triggered right at the CO₂ saturation plume front, potentially due to fluid–rock interaction effects. In addition, the seismic data highlighted subseismic faults that controlled the plume evolution. The Stage 3 experiment features an injection into the same geological formation with the same injection pressure and flow rate as the Stage 2C injection, and the active seismic data show that the two CO₂ plumes eventually merged together (Isaenkov *et al.*, 2022). Thus, one of the main achievements of our objectives of our study is to directly assess the value of information provided by the multiwell DAS array compared to a more standard areal monitoring array.

Here, we characterize the seismicity induced by CO₂ and brine injections by analyzing two years of passive DAS records. Microseismic analysis of the DAS data is still in its early days, and hence we first develop a set of new procedures for quantitative analysis of the DAS amplitudes. At the same time, we utilize prior analysis of the Stage 2C seismicity and repurpose the previously developed workflows for the new acquisition system. First, we scan several hundreds of terabytes of passive seismic records to identify the induced events. Then, we locate the events using travel-time inversion based on a velocity model from numerous vertical seismic profiling (VSP) surveys. After a calibration of the DAS amplitudes using regional catalogued earthquakes, we estimate the moment tensor of the sufficiently strong events. Finally, we analyze the triggering mechanism behind the main cluster of events by comparing patterns of induced seismicity against time-lapse VSP snapshots through the injection interval. This analysis confirms that the Stage 3 injection augmented and remobilized the Stage 2C plume.

Monitoring Data Set at Stage 3 of the Otway Project

The Otway International Test Centre is located at the coast of the Australian state of Victoria (Fig. 1a). In the past two decades, the site was established as an in situ research laboratory for GCS-related research with a focus on monitoring and verification technologies (Cook, 2014). Stage 3 was designed to test various approaches to cost-effective and low-invasive geophysical monitoring technologies for early detection of CO₂ leakage (Jenkins *et al.*, 2017). To this end, Stage 3 involved an injection of 15,000 tonnes of supercritical CO₂/CH₄ (80/20) mixture at 0.2 MPa pressure into the Lower Paaratte formation—a good quality sandstone reservoir at 1540 m depth below the ground.

The Stage 3 monitoring program consisted of VSP and pressure tomography surveys (Jackson *et al.*, 2021) using five deviated boreholes (CRC-3–CRC-7; Fig. 1b). The monitoring boreholes were instrumented by pressure gauges and high-SNR engineered optical fiber utilizing Silixa iDASv3 interrogators. The interrogators operated with 10 m gauge length, 4 m laser pulse length, pulse repetition frequency of 16 kHz, and the sampling rate of 1 kHz. The VSP program consisted of two elements: (1) repeat 3D VSP surveys after injection of 5000 and 10,000 tonnes of CO₂ with a vibroseis source (Yurikov *et al.*, 2022) and the DAS array, and (2) offset VSP surveys obtained every other day using permanent surface orbital vibrators (SOVs) and the DAS array (Isaenkov *et al.*, 2021; Pevzner *et al.*, 2022). Both the VSP techniques had high data repeatability and proved sensitive to the presence of CO₂. The 4D VSP provided a volumetric snapshot of the plume, whereas the SOV-DAS images sliced through the plume every 48 hr. These surveys confidently show that the Stage 3 plume remained inside the dedicated storage interval and reached the Stage 2C plume, which had been imaged by a time-lapse surface seismic inversion (Egorov *et al.*, 2017; Glubokovskikh *et al.*, 2019).

The pressure tomography included six surveys in total: three baseline injections, plus a survey after every 5000 tonnes of the CO₂ injection, for which each injection had between 1 and 2 MPa overpressure and lasted for a few hours (Jackson *et al.*, 2021). The pressure data show that the maximum pressure from the CRC-3 brine injections reaches CRC-6 and CRC-7 in less than a day. This implies that the pressure build-up induced by the CO₂ injection should occur in a matter of a few days as well. The VSP snapshots along with the pressure observations help us interpret the induced seismicity induced by the fluid injections for the Stage 3, experiment, as discussed in the next section.

Characterization of the Injection-Induced Events

Detection and location of the microseismic events

We acquired more than two years of passive records by the DAS systems in the five Stage 3 boreholes. To detect the induced microseismic events, we scan through several hundreds of

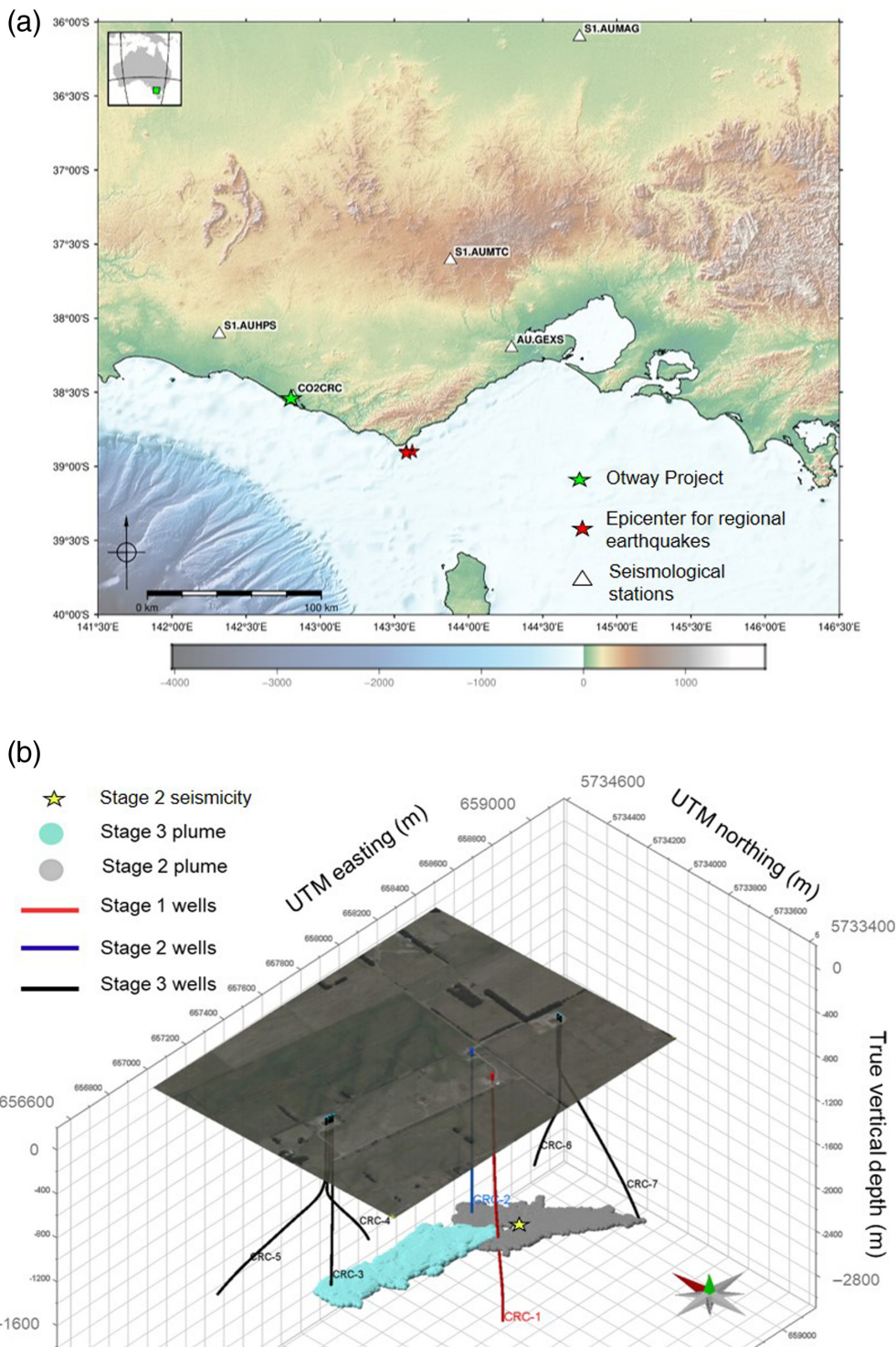


Figure 1. Outline of Stage 3 of the CO2CRC Otway Project. (a) We indicate the locations of the Otway in situ laboratory at the Victorian coast of Australia along with some relevant seismological stations and regional earthquakes. Inset in (a) shows a map of Australia, where the green marker identifies the location of the studied area. (b) The microseismic monitoring for Stage 3 relies on five monitoring boreholes (~1600 m depth) that were also the receivers for extensive time-lapse vertical seismic profiling (VSP) imaging of the Stage 3 plume. This plume has likely augmented the Stage 2 plume that was monitored using 909 buried vertical geophones and a VSP in CRC-1 well. The color version of this figure is available only in the electronic edition.

terabytes of the seismic data in two steps. First, we select several hundreds of the recorded segments with the ratio of short-time average/long-time average (STA/LTA) seismic energy, exceeding the background noise intensity—STA/LTA algorithm (Withers *et al.*, 1998). A visual review of these segments suggests that the majority of the triggers corresponds to the anthropogenic noise, natural earthquakes in deeper parts of the subsurface, and quarry blasts. However, the STA/LTA detected five template events (Fig. 2) for a subsequent semblance-based search using waveform cross correlation. This second iteration of the scanning picked up several tens of lower magnitude events. All of the detected signals were manually verified. We found only small number of low-magnitude events. Most likely, our detection workflow misses events that feature small, single-channel SNR. In fact, Figure 2 shows an undetected event 25 February 2021, which is clear visually. In addition, the SOV sweeps may have masked some events.

At the next step, we analyze the travel-time curves for the first arrivals of *P* and *S* waves to locate the seismicity hypocenters. The majority of the induced events feature a sufficient SNR for the first breaks picking in each of the five downhole DAS arrays, although the analysis in CRC-5 (the furthest from all hypocenters) and CRC-3 (due to the injection noise) is often challenging (Figs. 2, 3). Figure 3 shows that even a weak event can be seen on a DAS system located at least 1500 m away, despite relatively strong noise caused by injection

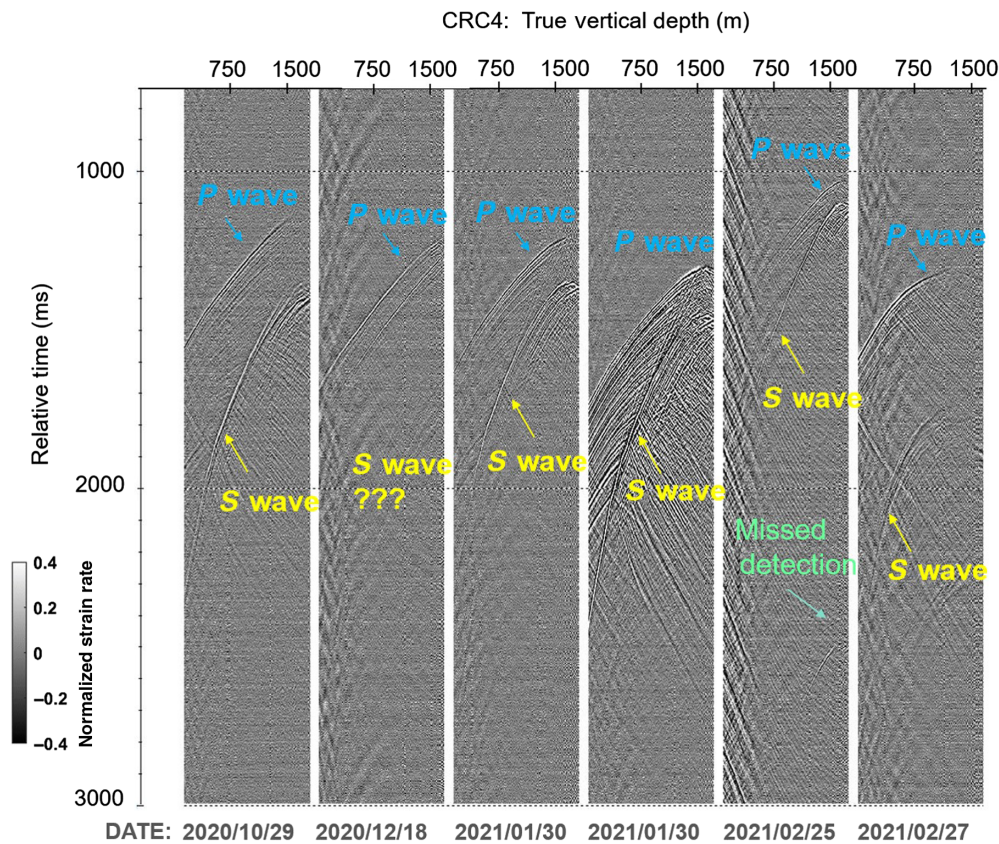


Figure 2. Seismograms in CRC-4 of the events detected during initial scanning through the passive seismic records using a channel-based energy detector. The second event (18 December 2020) is a local microearthquake unrelated to the injection. The other events were used as templates to the next iteration of the scanning. The color version of this figure is available only in the electronic edition.

operations. In addition, the first-arrival picks tend to have an increased uncertainty at the apex of the travel-time curves for three main reasons. First, the source mechanism for the majority of the events has a polarity flip in the vicinity of the apex. Second, *P*-wave amplitudes are attenuated by the directivity of the fiber optic sensors, which measure axial deformation of the cable. Third, the apexes feature an extremely complex structure of the recorded wavefield due to intense scattering and *P*- to *S*-wave conversion. Furthermore, the seismic properties have relatively strong anisotropy that manifests itself in splitting of the *S*-wave modes with different polarity. The mode with horizontal polarity can only be seen in the deviated segments of the monitoring boreholes and disappears in the vertical segments of the fiber optic cables. This fact becomes even more obvious after a conversion of the DAS measurements into displacements, as discussed in the next section.

Having obtained first-break picks, we located the microseismic events using a velocity model obtained from the analysis of the numerous VSP surveys at the Otway site. The 3D VSP data acquired at the Otway site show that in addition to polar anisotropy of the subsurface with a vertical axis symmetry,

seismic velocities have some degree of azimuthal anisotropy aligned with the maximum horizontal stress and predominant orientation of the faults (Popik *et al.*, 2020). However, the VSP illuminates the subsurface along ray paths that originate at the surface and propagate at reservoir depths with relatively small angle with respect to the vertical. Thus, these travel times do not allow building an accurate anisotropic velocity model suitable for microseismic signals that originate at reservoir depth and propagate near horizontally to the DAS wells. Instead, we use a 1D model calibrated to numerous offset SOV-DAS VSP surveys that only accounts for the polar anisotropy (Alkhalifah and Tsvankin, 1995). Finally, we implemented a two-step events location workflow. First, the location algorithm estimates the hypocenters at the mean apex depth for the *P* wave in the five boreholes, whereas the lateral location follows from $(t_S - t_P)$

—the delay between the *P* and fast *S* waves (Fig. 3). This hypocenter was used in a grid search to minimize the mean-squared time residuals. The search always provided a single and clear minimum. Figure 4 shows the initial and final locations for the two strongest microseismic events. We see that the elliptic contours of the same time residuals are elongated in the southwest–northeast direction, orthogonally to the longer axis of the plume, which means that the lateral hypocenter location is relatively uncertain in this direction. The depths of the hypocenters may be relatively confidently attributed to the injection interval.

It is hard to establish an unambiguous causal link between the occurrence of a microseismic event and the injection. Perhaps, the strongest evidence is that the fluid-induced events occur at reservoir depth relatively close to the CO₂ plumes either during an injection or immediately after one. Overall, our detection and location workflow attributed 17 events to the Stage 3 fluid injections of brine and CO₂.

Microseismic source mechanisms

The distribution of the first motions of the *P* and *S* waves throughout the DAS array reflects the configuration of the

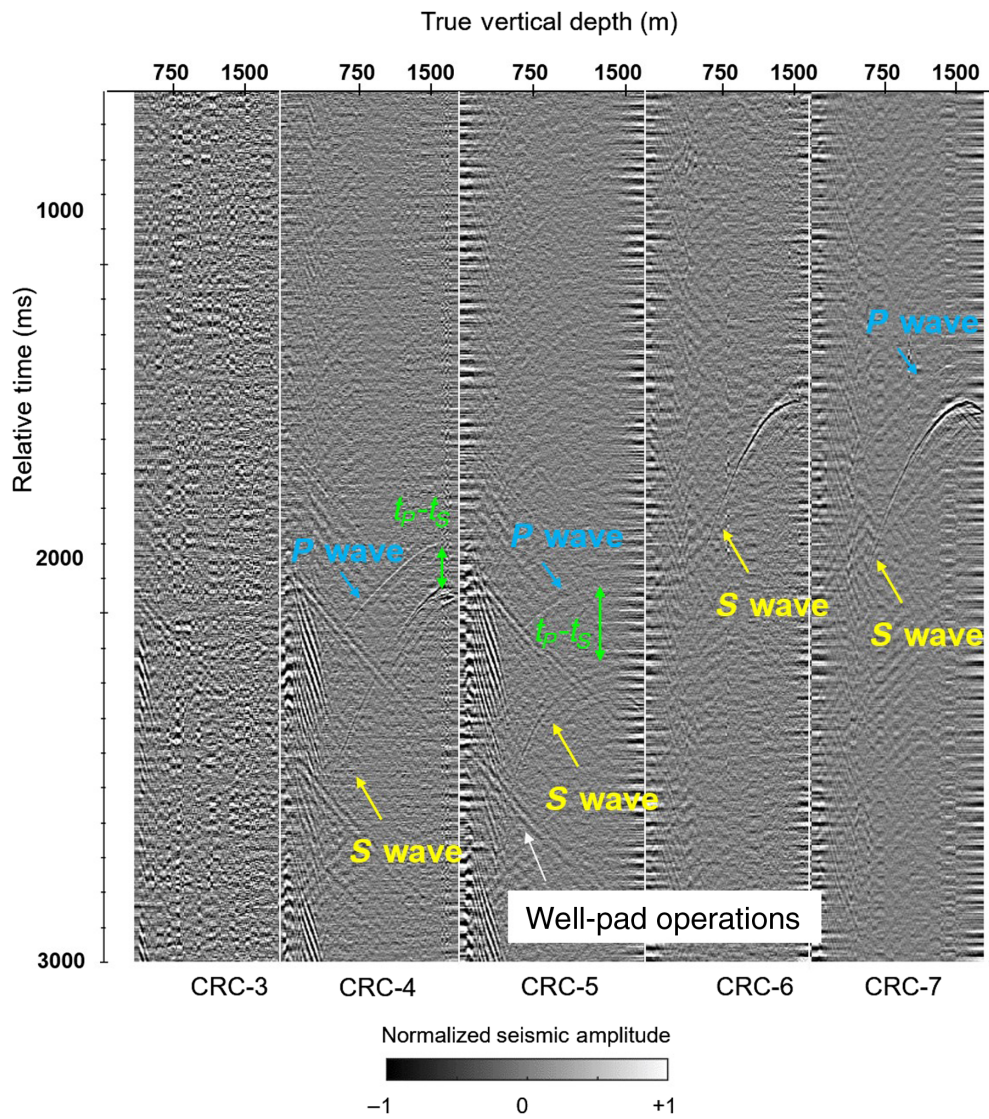


Figure 3. Strain-rate seismogram for event 16—one of the weakest microseismic events with $M_w \sim -2$. The distributed acoustic sensing (DAS) array has sufficient sensitivity to pick the first P - and S -wave arrivals in all five boreholes. The color version of this figure is available only in the electronic edition.

reactivated faults and the slip along the fault, which is traditionally expressed through seismic moment tensor $\hat{\mathbf{M}}$. For a homogeneous but lossy medium, the relationship between the $\hat{\mathbf{M}}$ and displacement vector $\vec{\mathbf{u}}$ is (Shearer, 2019)

$$\vec{\mathbf{u}} = \left(\frac{\partial/\partial t \hat{\mathbf{M}}(t-r/c) \cdot \vec{\mathbf{k}}}{4\pi\rho c^3 r} \exp[-\pi f_0 r/Qc] \right) \cdot \hat{\mathbf{P}},$$

$$\hat{\mathbf{P}} = \begin{cases} (\vec{\mathbf{k}} \otimes \vec{\mathbf{k}}) & \text{for } P \text{ wave,} \\ (\hat{\mathbf{I}} - \vec{\mathbf{k}} \otimes \vec{\mathbf{k}}) & \text{for } S \text{ wave} \end{cases}, \quad (1)$$

in which $\vec{\mathbf{k}}$ is a unit vector in the direction of the wave propagation, ρ is the bulk density, c is a propagation velocity of P or S waves, r is a distance to the receiver, and t is the time counting from the event's triggering, $\hat{\mathbf{I}}$ is a metric tensor, coordinates of

which become a unit matrix in a Cartesian coordinate system, \otimes denotes tensor product of vectors, and \cdot denotes dot product. In equation (1), the exponential factor accounts for the attenuation for straight-ray wave propagation, in which the quality factor $Q = 90$ was estimated from numerous VSP surveys at the site (Pirogova *et al.*, 2019) and a central frequency f_0 for a particular microseismic event (usually, ~ 100 Hz).

We analyse P -wave first motions to estimate the strike and dip of the reactivated faults and the relative movement of the fault wall—direction of the slip relative to the fault strike, which is referred to as rake. We assume a pure double-couple nature of the microseismic source mechanisms to stabilize the focal mechanism estimation, given the limited angular coverage of the DAS array. Previously, this assumption was found to be a reasonable approximation for the Stage 2C seismicity (Glubokovskikh *et al.*, 2022). We start by converting the DAS records, axial strain rate, to the axial displacements, which is also required for the magnitude estimation in the next section. The conversion workflow for iDASv3 is presented

in detail in Glubokovskikh *et al.* (2021). Effectively, the conversion implements a time and spatial integration of the data, so the axial displacement seismograms have lower frequency signals and lower SNR compared to the strain-rate seismograms.

Our final inversion workflow searches for a match between the amplitudes of the first maximum P -wave displacements extracted along the picked travel-time curves (Fig. 5a). As at this stage we are not trying to estimate event magnitudes, we normalize the displacements to the maximum value among all boreholes. Initially, we implemented a simple grid search through the 3D space, strike/dip/rake, to minimize the mean-squared error $\text{rms}(u_p^o - u_p^m)$ between the observed u_p^o and modeled amplitudes u_p^m . However, the error surface contains several local minima due to the presence of noise in the data

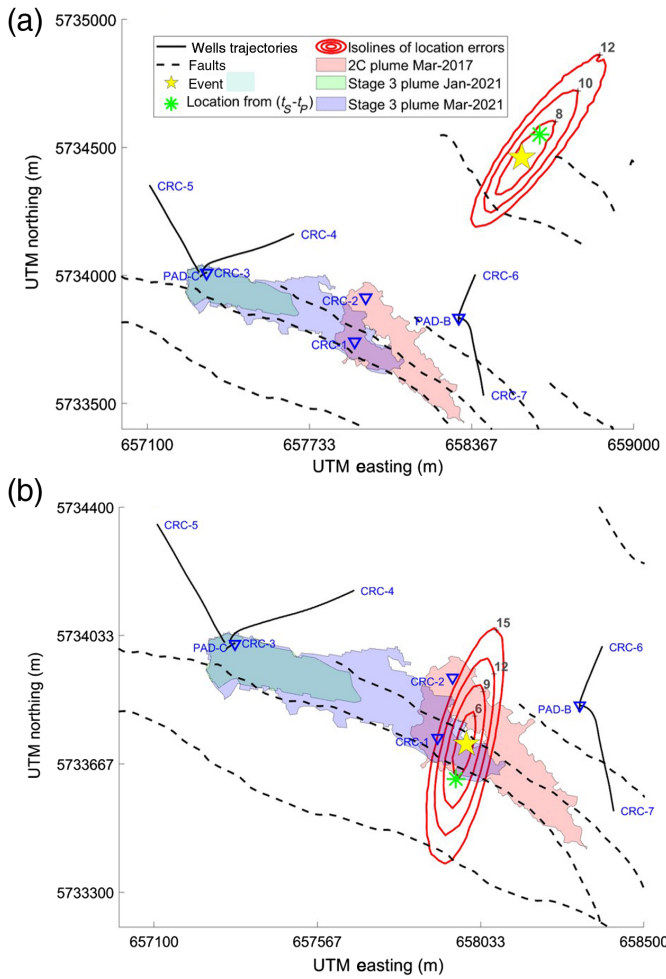


Figure 4. Location of the epicenters of the strongest microseismic (a) event 21 and second strongest microseismic (b) event 5. The initial location (green asterisk) was obtained from $t_s - t_p$ delay, which is shifted laterally relative to the final location (yellow star) obtained through a travel-time inversion. The direction of the lateral shift is consistent with the structure of the inversion uncertainty: red ellipses correspond to the isolines of the mean-squared discrepancy between the theoretical and observed travel-time curves, with black numbers indicating the error values in millisecond. The color version of this figure is available only in the electronic edition.

and imperfect amplitude picks. To regularize the inversion, we assigned higher weights w_k to data from the CRC-4, CRC-6, and CRC-7 wells, which are closer to all of the hypocenters, and thus have higher SNR and more robust travel-time picks. In addition, the objective function included a regularization term that penalized the opposite signs between u_p^o and u_p^m to force the inversion algorithm to honor the polarity flips:

$$\mathcal{L}u_p = \sum_{k=\text{CRC-3}}^{\text{CRC-7}} w_k \text{rms}(u_p^o - u_p^m) + \alpha_k \text{ReLU}(-u_p^o \cdot u_p^m),$$

$$\text{ReLU}(-u_p^o \cdot u_p^m) = \begin{cases} (u_p^o \cdot u_p^m), & \text{for large observed } u_p \text{ and incorrect inverted polarity,} \\ 0, & \text{when observed and inverted } u_p \text{ are of the same sign,} \end{cases} \quad (2)$$

in which the weights w_k and α_k for CRC-3 and CRC-5 were from two to three times smaller than for the high-SNR wells CRC-4, CRC-5, and CRC-7. Glubokovskikh *et al.* (2022) implemented a somewhat similar approach to focal mechanism estimation, honoring the polarity flips for the microseismic events recorded by surface vertical geophones.

Figure 5b shows that the inverted P -wave displacements capture relatively well the amplitude distribution along the boreholes as well as the location of the polarity flips in all of the boreholes. For a qualitative validation of the inverted dip/azimuth/rake values, we compare the predicted S -wave displacements against the observations (Fig. 5c). The agreement is generally good, except for the vicinity of the S -wave apexes, for which, as discussed earlier, the first-break picks are challenging. Thus, we conclude that the double-couple approximation is consistent with the data.

Estimation of the moment magnitude

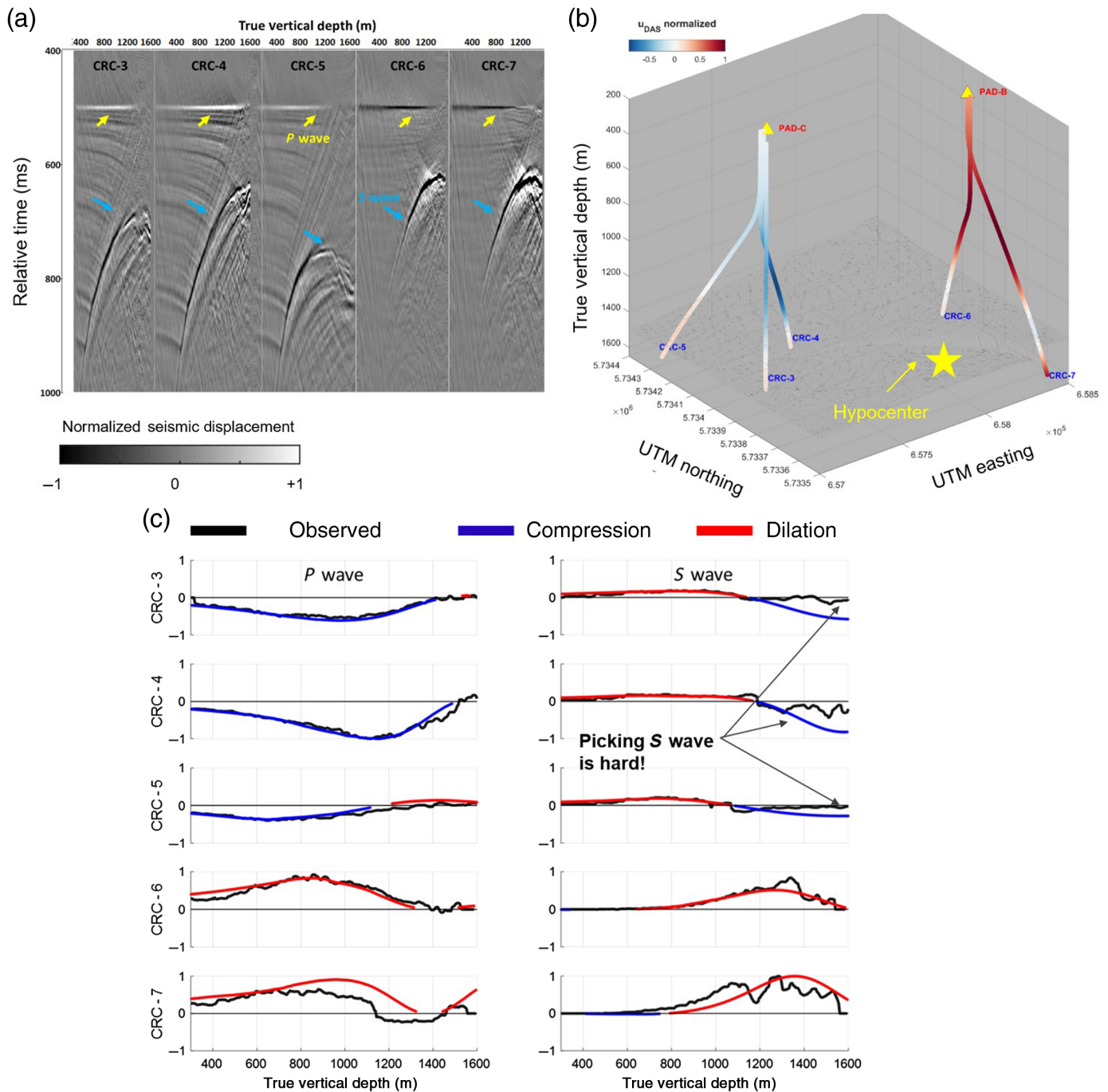
Magnitude is a standard metric of strength of a seismic event, whether an earthquake or microearthquake, and characterizes both the size of a reactivated fault and slip along its surface. Observational seismology defines the magnitude using various empirical relationships (Shearer, 2019), which rely on a handful of the seismic waveform parameters, such as maximum amplitude and visible period. For example, local magnitude M_L is defined as

$$M_L = \log_{10}(\max u_z) + 2.56 \log_{10}(R) - 1.67, \quad (3)$$

in which $\max u_z$ denotes the maximum vertical displacement in micrometers for a given seismic event, R is a distance to the hypocenter in kilometers. This relationship was derived from seismological catalogs of regional earthquakes with $M_L > 2$ and $10 \text{ km} < R < 500 \text{ km}$. Hence, this and similar equations might be inapplicable to reservoir-scale microseismic monitoring, which features much smaller distances and magnitudes; although there are several examples of such applications (e.g., Lellouch *et al.*, 2020). Instead, following the strategy employed for the Stage 2C seismicity (Glubokovskikh *et al.*, 2022), we use the seismic moment magnitude M_w that is directly related to the norm M_0 of the seismic moment tensor

$$M_w = 2/3(\log_{10}(M_0) - 9.1). \quad (4)$$

To this end, we fit the events spectra $A(f)$ compensated for the propagation loss and radiation pattern according to



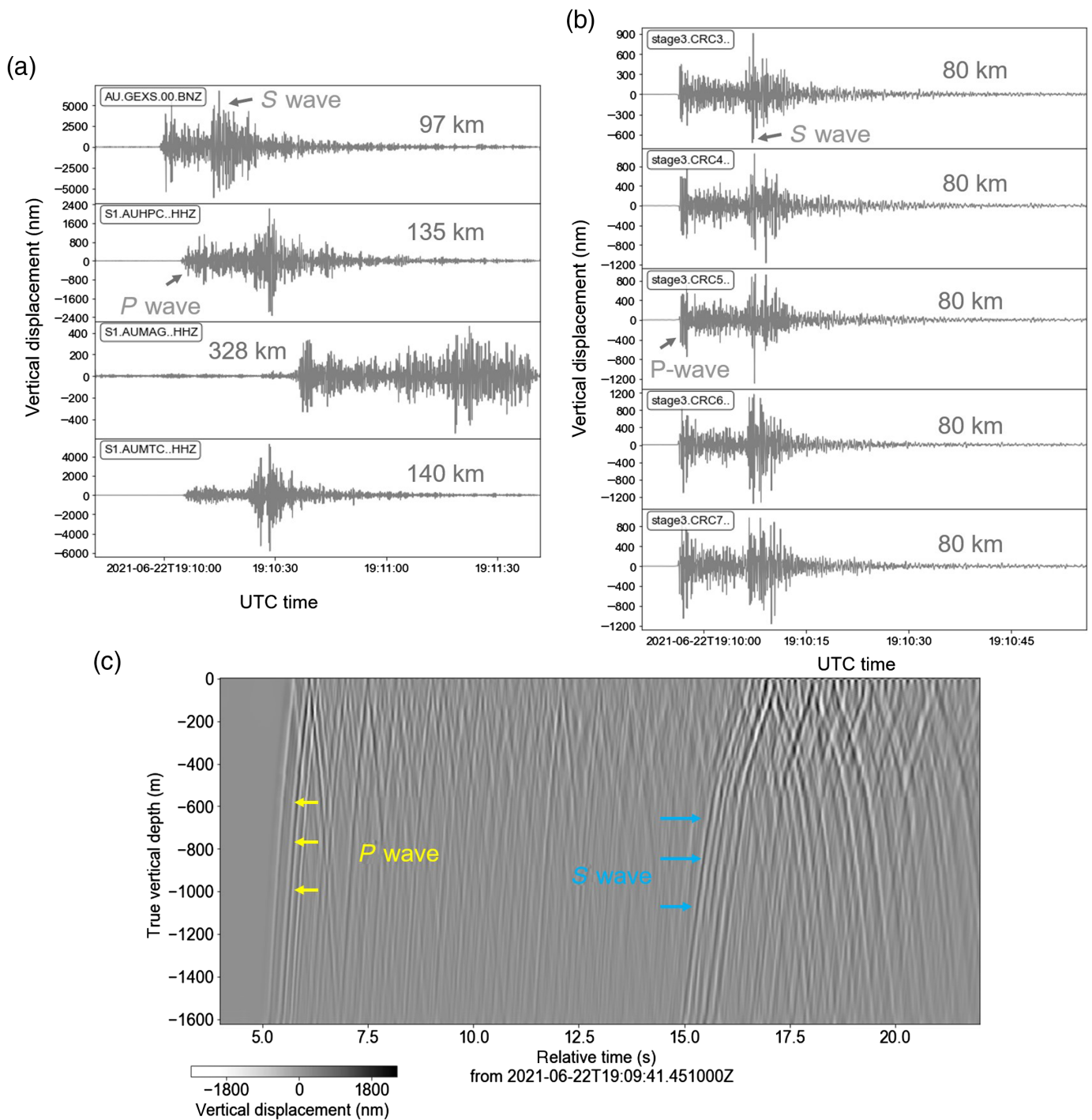
equation (1) to the model of Brune (1970),

$$A(f) = \frac{M_0}{4\pi\rho c^3(1 + f/f_c)^2}, \quad (5)$$

in which spectral level at the low-frequency limit depends on the size of the fault and slip, and f_c is the corner frequency controlled by the fault size.

Equation (5) assumes that the DAS system is perfectly coupled to the surrounding formation. This hypothesis, however, contradicts the published studies of the instrument response for DAS systems (Lindsey *et al.*, 2020; Paitz *et al.*, 2020). Glubokovskikh *et al.* (2021) that the DAS in CRC-3 has

Figure 5. An illustration of the workflow for focal mechanism estimation—event 5. (a) We rely on the spatial variation of the maximum amplitude of the first *P*-wave arrivals, which are flattened in the DAS seismograms converted to vertical polarity changes for the *P* waves. (b) The monitoring boreholes contain several polarity changes for the *P* waves. (c) These changes allowed us to constrain the inversion of the configuration of the reactivated fault and slip direction. Note that *S*-wave amplitudes did not participate in the inversion; we show them as a qualitative confirmation of the inverted parameters. We may see that picking the *S* waves near the apices is challenging (a). The color version of this figure is available only in the electronic edition.



20 dB lower intensity of the ocean-generated microseisms (below 2 Hz) compared with a calibrated broadband seismometer located relatively close to the site. The majority of existing studies suggest that the reduced sensitivity is caused by the interaction between the fiber and other components of the cable. The coupling may only be estimated empirically. We use the records at four calibrated seismological stations for the three regional earthquakes with $M_L > 3$ originating at a shallow depth (~ 10 km) offshore Apollo Bay, Victoria (Fig. 1a). Essentially, we compare the local magnitude determined from the converted downhole DAS measurements against that obtained from seismological

Figure 6. Appearance of a regional earthquake M_L 3.6 that occurred in the Apollo Bay (Victoria, Australia) on 22 June 2021 (see Fig. 1a). (a) The waveforms recorded by vertical components of selected seismological stations are converted to the displacements. (b) In the Stage 3 wells, the earthquake looks almost identical at 700 m depth channel as well as in the (c) entire interval 600–800 m that is being used for the magnitude estimation. Note that the maximum amplitudes on the DAS sensors are considerably smaller than on the seismological stations located further away from the hypocenter. The color version of this figure is available only in the electronic edition.

TABLE 1

Catalog of the Local Magnitudes M_L for the Three Regional Earthquakes from Apollo Bay (Victoria, Australia) Shown in Figure 1

Date and Time (yyyy/mm/dd hh:mm:ss) (UTC)	Catalog M_L	Station	Distance (km)	P -Wave M_L	S -Wave M_L
2020/08/17 12:35:49	3.2	AU.GEXS	96	3.3	3.52
		S1.AUMAG	322	3.1	3.64
		S1.AUMTC	145	3.16	3.86
		S1.AUHPC	142	3.22	3.4
		CRC-3	79	2.17	2.1
		CRC-6	79	2.5	2.7
2021/06/22 19:09:41	3.64	AU.GEXS	97	4.22	4.28
		S1.AUMAG	330	4.35	4.6
		S1.AUMTC	140	3.85	4.6
		S1.AUHPC	135	3.63	4.2
		CRC-3	80	2.9	3.1
		CRC-6	80	3.1	3.2
2021/06/22 19:23:53	3.3	AU.GEXS	97	3.37	4.64
		S1.AUMAG	328	3.6	3.95
		S1.AUMTC	140	3.17	3.8
		S1.AUHPC	135	3.2	3.45
		CRC-3	79	2.2	2.2
		CRC-6	79	2.45	2.4

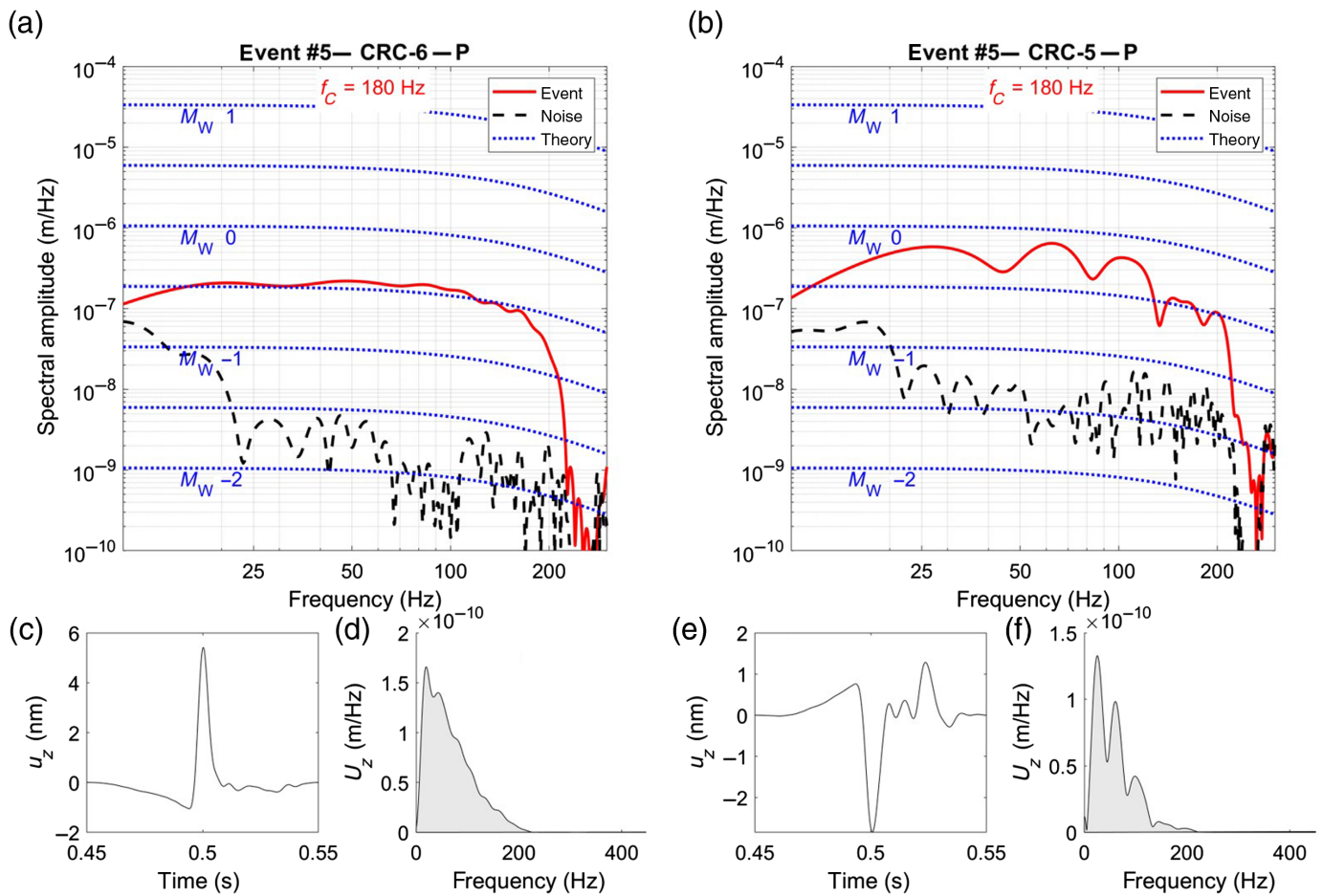
stations (Fig. 6), summarized in Table 1. In the analysis, we give more weight to the M_L estimates obtained at S1.AUHPC station, because it belongs to the same wave propagation path as the CRC wells, and thus should have a similar overprint of the source function and propagation losses.

We estimate the earthquakes magnitudes in CRC-3 and CRC-7 using a stacked P -wave wavelet in the interval 600–800 m true vertical depths. We chose this interval, because it features (1) relatively uniform formation stiffness and its effect on the amplitudes (Pevzner, Gurevich, *et al.*, 2020; Shashkin *et al.*, 2022); (2) most reliable travel-time picks with neither polarity flips nor interference of various wave modes; (3) nearly vertical borehole trajectories, which simplifies the correction for the radiation pattern. Table 1 suggests that the DAS response should be multiplied by a factor of 8 to bring the P -wave magnitudes in agreement with the S1.AUHPC estimates. Strictly speaking, this DAS sensitivity should be frequency dependent; but accounting for this would require a broadband calibrated seismic signal, which is not available. Our approach implies that the same factor would be relevant throughout a relatively wide frequency range (10–250 Hz) typical for the detected events. The data show that the P -wave magnitudes are relatively consistent for the five boreholes

(Fig. 7). The estimates of the corner frequency for some of the events are problematic, because the passive records were resampled to 2 ms for the sake of frugal data storage, which is insufficient for some of the higher frequency wavelets. In addition, 10 m gauge length may preclude adequate sampling of higher frequencies. Thus, the estimates of the corner frequency have relatively high uncertainty, and the rolloff of the spectrum in Figure 7 is much steeper than f^{-2} assumed in the theoretical model in equation (5).

Analysis of the Results

Table 2 and Figure 8 summarize the quantitative characteristics of the fluid-induced seismicity during the Stage 3 experiment. The strongest event has M_w 0.1. Figure 3 shows event 16—one of the weakest events $M_w \sim -2$, which can be seen in the CRC-5 well located at least 1500 km away. This event was detected despite strong injection noise, because for detection of smaller events we used a higher frequency range, for which these smaller events have higher SNR. The lowest quantifiable events have $M_w > -1.5$. A somewhat unexpected observation is a disproportionately small number of low-magnitude events. This might be due to insufficiently sensitive events detection workflow and limitations of the acquisition system: the large



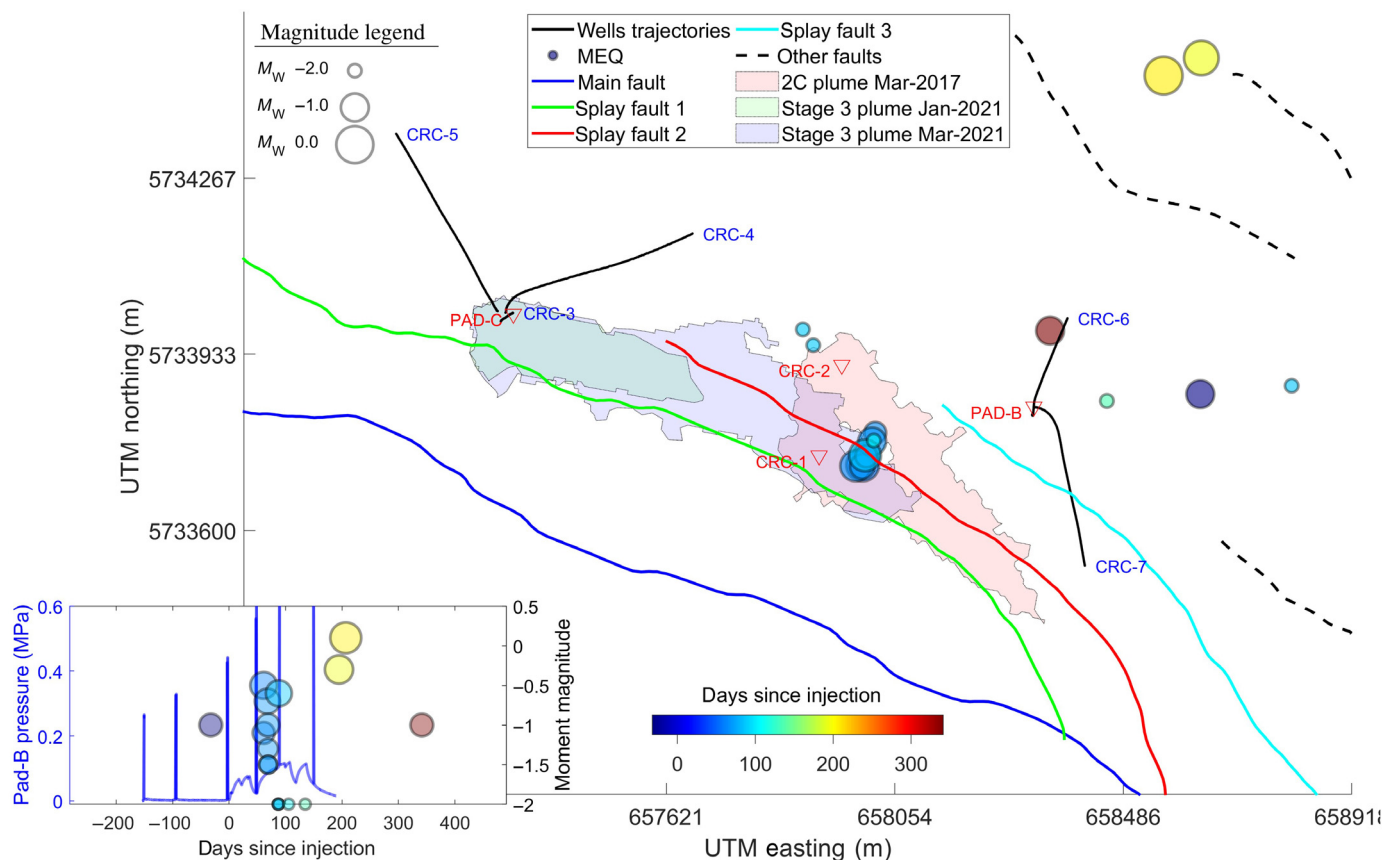
gauge length and insufficient temporal sampling complicated detection of smaller events, which usually have higher corner frequencies.

According to their hypocenters and source mechanisms, the induced events may clearly be split into four groups. The main cluster of nine events occurs at a small patch at Splay Fault 2 inside the gap in the Stage 2C plume. Another two events occurred close to the CRC-2 well, at the edge of the seismically visible Stage 2C plume. Then, some of the events occurred outside of the Stage 3 and Stage 2C saturation plumes: two strong events occurred to the north from the Well Pad B two months after the end of the CO₂ injection; a group of several events were detected close to the Well Pad B without any clustering in space–time, although we were unable to trace any faults aligned with the hypocenters. The majority of such events seems to be related to the brine injections for the purpose of time-lapse pressure tomography through the plume and may have been triggered by pressure front alone.

We found both similarities and differences between the microseismic responses for the Stage 2C and Stage 3 injections. Figure 9 shows close similarity between the seismicity induced by the Stage 2C and Stage 3 injections. These clusters are located at Splay Fault 2 and are aligned perpendicular to that fault, and the offset between the events might be a result of inaccuracies of

Figure 7. Illustration of the magnitude estimation for event 5, $M_w = 0.5$, located within Stage 2C plume. We only show (a,c,d) CRC-6 and (b,e,f) CRC-5, which has the highest and the lowest signal-to-noise ratio (SNR), respectively. To increase the SNR, we stack the wavelets along 600–800 m true vertical depth (40 channels). (a,b) Then, the magnitude estimates resulted from fitting the spectra corrected for wave energy losses and radiation pattern to equation (5). We also show (c,e) the raw waveform for axial displacement u_z and (d,f) corresponding frequency spectra U_z . The color version of this figure is available only in the electronic edition.

the velocity model. The source mechanism of the Stage 3 events coincides with that of the Stage 2C events that were observed close to the end of that injection. Both the injections produced events on a fault with southwest–northeast orientation, orthogonal to the seismically visible faults that contact with the CO₂ plumes. At the same time, Stage 3 featured some events triggered by the pressure outside the plumes, which were not detected in the Stage 2C data. This difference may be due to the lower sensitivity of the Stage 2C array and related differences between the two workflows. Indeed, to compensate for the lack of sensitivity of the buried array of vertical geophones, the Stage 2C workflow (Glubokovskikh *et al.*, 2022) incorporated spatial filters



suppressing events that originated away from the immediate proximity of the Stage 2C plume. In contrast, DAS arrays employed in Stage 3 have much lower detection threshold and thus did not require such spatial filters.

Seismicity at Stage 2C and Stage 3 was triggered by a relatively small pressure perturbation expected at several hundred meters away from a well with ~ 200 kPa injection overpressure. To estimate the lower bound for the critical pressure that reactivated the fault, we use the fact that brine and supercritical CO_2 are nearly immiscible, and brine is a wetting phase for the Lower Paaratte sandstones whereas CO_2 is not (see subsection 6.5 in Cook, 2014). Thus, the plume front must overcome some capillary pressure p_C to replace brine in a pore channel of radius r_C ,

$$p_C = \frac{2\sigma_C \cos \theta_C}{r_C}, \quad (6)$$

in which σ_C and θ_C are interfacial tension and wetting angle, respectively, for the system CO_2 -brine-rock. These values depend on lithology, composition of the brine, and reservoir conditions. However, variability of these parameters for the Stage 3 injection may change the value of capillary pressure by a factor of 2, not by an order of magnitude (Saraji *et al.*, 2013; Sarmadivaleh *et al.*, 2015). By assuming the values, $\sigma_C \sim 30$ mN/m and $\theta_C \sim 30^\circ$ (see subsection 6.5 in Cook, 2014) and $r_C \sim 10$ μm , the minimum pressure inside the plume should be ~ 5 kPa. This pressure

Figure 8. Illustration of the full catalog of detectable microseismic events that may be confidently attributed to the fluid injections for Otway Stage 3 experiment. The inset figure in the bottom left corner shows the mean pressure gauge readings at the well pad B, for which the spikes correspond to brine injections for the pressure tomography, and a continuous anomaly corresponds to the pressure plume produced by the CO_2 injection. The color version of this figure is available only in the electronic edition.

may be sufficient to trigger the microseismic events on a critical fault adjacent to the Splay Fault 2, because it exceeds the strength of earth tides as well as the strongest ambient seismic noise signals at the site (Glubokovskikh *et al.*, 2021; Shashkin *et al.*, 2022) that have reactivated the seismogenic faults with lower critical pressure. In addition, Rotherth and Shapiro (2007) showed that fluid-induced seismicity may be triggered by fluid pressure just above 1 kPa.

Glubokovskikh *et al.* (2022) suggested that the Stage 2C events might indicate the importance of chemical reactivation of the seismogenic fault by the acidified brine. The main argument was that all of the events occurred at the fault within one week after the plume arrival to an intact portion of the fault gouge material. Figure 10 shows that the timing of the Stage 3 events also follows the evolution of the CO_2 plume, because it was imaged by the time-lapse anomalies in the DAS-VSP

TABLE 2

Catalog of the Microseismic Events Induced by the Brine and CO₂ Injections during the Stage 3 Experiment

Number	Date and Time (yyyy/mm/dd hh:mm) (UTC)	UTM East (m)	UTM North (m)	Depth (m)	M_w	f_c (Hz)	Strike/Dip/Rake (°)
2	2020/10/29 02:29	658631.5	5733858	1490	-1	90	70/30/270
4	2021/01/30 16:55	657999.1	5733742	1470	-1.1	180	40/70/270
5	2021/01/30 18:46	657992.4	5733723	1470	-0.5	180	40/70/270
6	2021/02/06 10:41	657979.2	5733722	1450	-0.7	180	40/70/270
7	2021/02/07 13:19	657991.7	5733721	1450	-1.3	130	40/70/270
8	2021/02/07 14:20	658016.3	5733785	1430	-1.5	110	40/70/270
9	2021/02/07 14:21	658010.5	5733768	1450	-1	150	40/70/270
10	2021/02/07 15:48	657999.4	5733740	1470	-1.5	150	40/70/270
11	2021/02/25 20:23	658804.5	5733873	1510	Nan	Nan	Nan
12	2021/02/25 22:10	657879.3	5733980	1470	Nan	Nan	Nan
13	2021/02/25 23:10	657899	5733950	1470	Nan	Nan	Nan
14	2021/02/26 09:39	657997	5733742	1470	-0.6	180	215/20/270
16	2021/03/16 01:54	658013.6	5733770	1450	Nan	Nan	Nan
18	2021/04/14 08:58	658454.8	5733845	1470	Nan	Nan	Nan
20	2021/06/13 05:11	658633.5	5734494	1490	-0.3	140	35/10/265
21	2021/06/25 05:48	658562.1	5734460	1450	0.1	140	35/10/265
24	2021/11/06 23:35	658347.3	5733978	1450	-1	120	Nan

Nan, the signal-to-noise ratio is insufficient for accurate estimation of the parameters.

snapshots (Isaenkov *et al.*, 2022) as well as 4D VSP (Yurikov *et al.*, 2022). In particular, all of the events from the main seismicity cluster occurred only after the Stage 3 plume reached and augmented the Stage 2C plume: Figure 10a–c shows time-lapse seismic features A–C that indicate the movement of Stage 2C plume. This remobilization of the plume coincided in time and space with new triggered events. In addition, feature D in Figure 10d indicates that the Stage 2C plume eventually moved and reached the CRC-7 well. The 3D VSP plume contours support this interpretation. We believed that the two CO₂ injections at the Otway site clearly confirmed the fact that the movement of CO₂ through Splay Fault 2 produced a weakening effect on the fault. However, the effect of carbonic acid on the mechanical properties of reservoir rocks is assumed to be very small (Rohmer *et al.*, 2016); thus the weakening mechanisms requires a thorough corroboration by laboratory studies.

The two discussed mechanisms, capillary entry pressure and geochemical reactions, are complementary and may both contribute to the observed onset of the microseismic effects at the front of the CO₂ saturation plume. The scale of these effects may be relatively small, as we do see that the small pressure increase outside of the plumes was still sufficient to trigger seismicity in the storage formation.

Conclusions

We presented the results of microseismic monitoring of a small-scale injection of supercritical CO₂-rich mixture for the Stage 3 Otway Project using a unique multiwell DAS array. We developed a workflow for quantitative characterization of microseismic events using DAS data from a set of deviated boreholes. Thanks to the dense spatial sampling by the DAS, we were able to estimate the focal mechanisms for events with $M_w > -1.5$, although the monitoring boreholes provided very limited angular coverage. To calibrate the amplitudes on DAS, we estimated the coupling factors using regional earthquakes and available seismological stations. The DAS array has sensitivity sufficient for detection and location of induced events with $M_w \sim -2$, which occurred up to 1500 m away from a monitoring borehole.

The observed induced seismicity may be split into two categories: (1) associated with the CO₂ saturation plume evolution and (2) occurring outside of the plume. The strongest events from the first category are collocated with the events triggered by a previous injection (of the Stage 2C Otway Project). The focal mechanisms of the two injections coincide with each other. The events triggered by the Stage 3 injection within the Stage 2C plume were directly related to the CO₂ flow. The distribution of the microseismic events in space and time follows closely the time-lapse anomalies evident in the

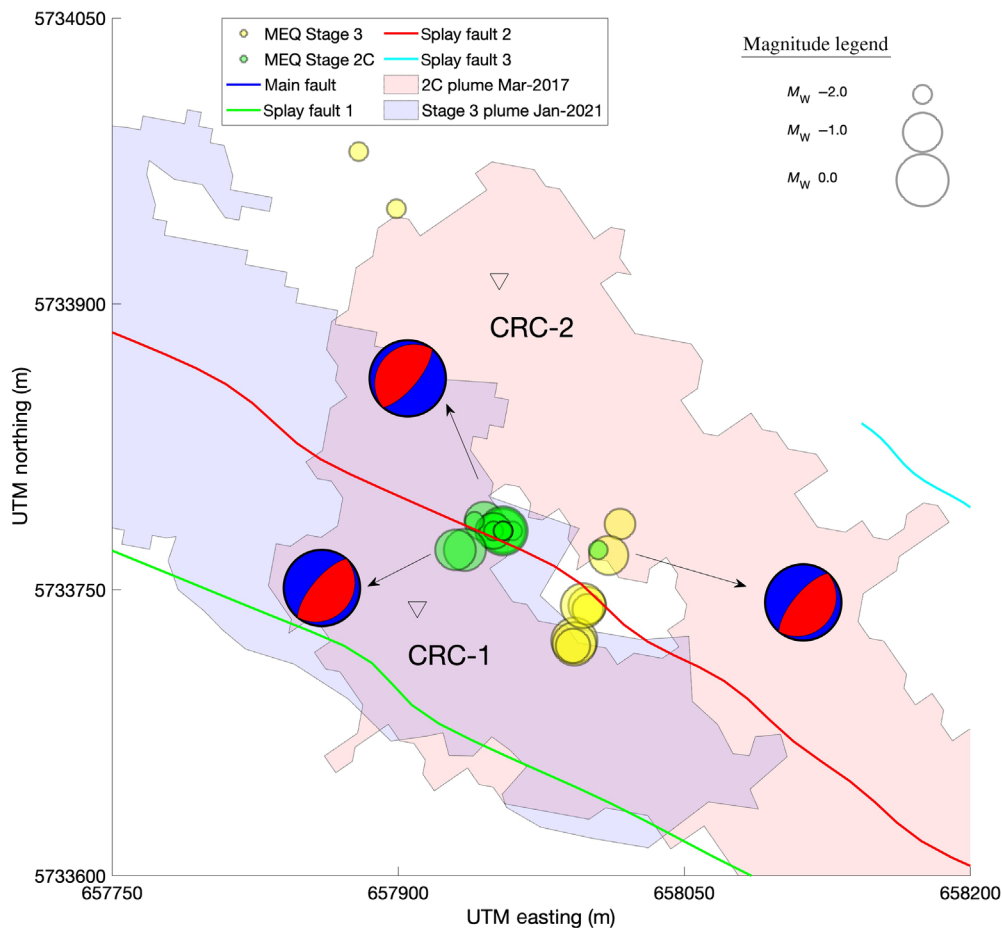


Figure 9. Comparison of the main seismicity clusters induced by Stage 2C and Stage 3 injections. Stage 2C included two bursts of seismicity (north and south side of splay fault 2) that lasted for one day that featured different focal mechanisms. All quantifiable Stage 3 events have the same focal mechanism as the latest Stage 2C seismicity cluster. The color version of this figure is available only in the electronic edition.

snapshots of the injection interval provided by the 3D and offset VSP. We observed a similar behavior of the same fault patch during the Stage 2C injection. The second type of events occurred outside of the zones saturated by CO₂. Most of these events seem to be related to the brine injections for time-lapse pressure tomography through the plume.

The nature of the plume-fault interaction remains unclear, but chemical alteration of the fault gouge might have reduced the faults' stiffness and made them more prone to reactivation by the pressure perturbation. Importantly, the seismogenic fault was not traceable in the seismic images. Only DAS observations revealed this fault as well as a fluid-rock interaction, which may control the CO₂ flow. Thus, we conclude that microseismic monitoring using multiwell DAS systems may provide relatively inexpensive but sensitive tool that may improve our understanding of the complex thermal, mechanical, and chemical processes accompanying CO₂ storage operations.

Data and Resources

The seismic records for all the 17 injection-induced seismic events are available at <https://doi.org/10.5281/zenodo.7574468>. The full data set supporting this research is available in the Centre for Exploration Geophysics at Curtin University and CO2CRC Limited (<https://co2crc.com.au/>) owns the data set. Access to the full data set may be granted by the company and will be subject to review upon request sent through this link <https://co2crc.com.au/contact/>. The regional earthquakes data detailed here are archived and publicly accessible through the Incorporated Research Institutions for Seismology (IRIS). Waveform retrieval was done using the International Federation of Digital Seismograph Networks (FDSN) client functionality in ObsPy (Beyreuther *et al.*, 2010). Some plots were made using the Generic Mapping Tools (GMT) version 4.2.1 (www.soest.hawaii.edu/gmt/; Wessel and Smith, 1998). All websites were last accessed in June 2023.

Declaration of Competing Interests

The authors acknowledge that there are no conflicts of interest recorded.

Acknowledgments

The Otway Project received CO2CRC Ltd. funding through its industry members and research partners, the Australian Government under the CCS Flagships Programme, the Victorian State Government, and the Global CCS Institute. The authors wish to acknowledge financial assistance provided through Australian National Low Emissions Coal Research and Development. ANLEC R&D is supported by Low Emission Technology Australia (LETA) and the Australian Government through the Department of Industry, Science, Energy, and Resources. PAWSEY Supercomputing Center provided them with access to their high-performance computing facilities, which made this work possible. Boris Gurevich and Serge Shapiro acknowledge support from the Australian Research Council through Project Number DP190103260. Stanislav Glubokovskikh acknowledges the support provided by the Office of Fossil Energy and Carbon Management of the U. S. Department of Energy (DOE) through Core Carbon Storage and Monitoring Research project.

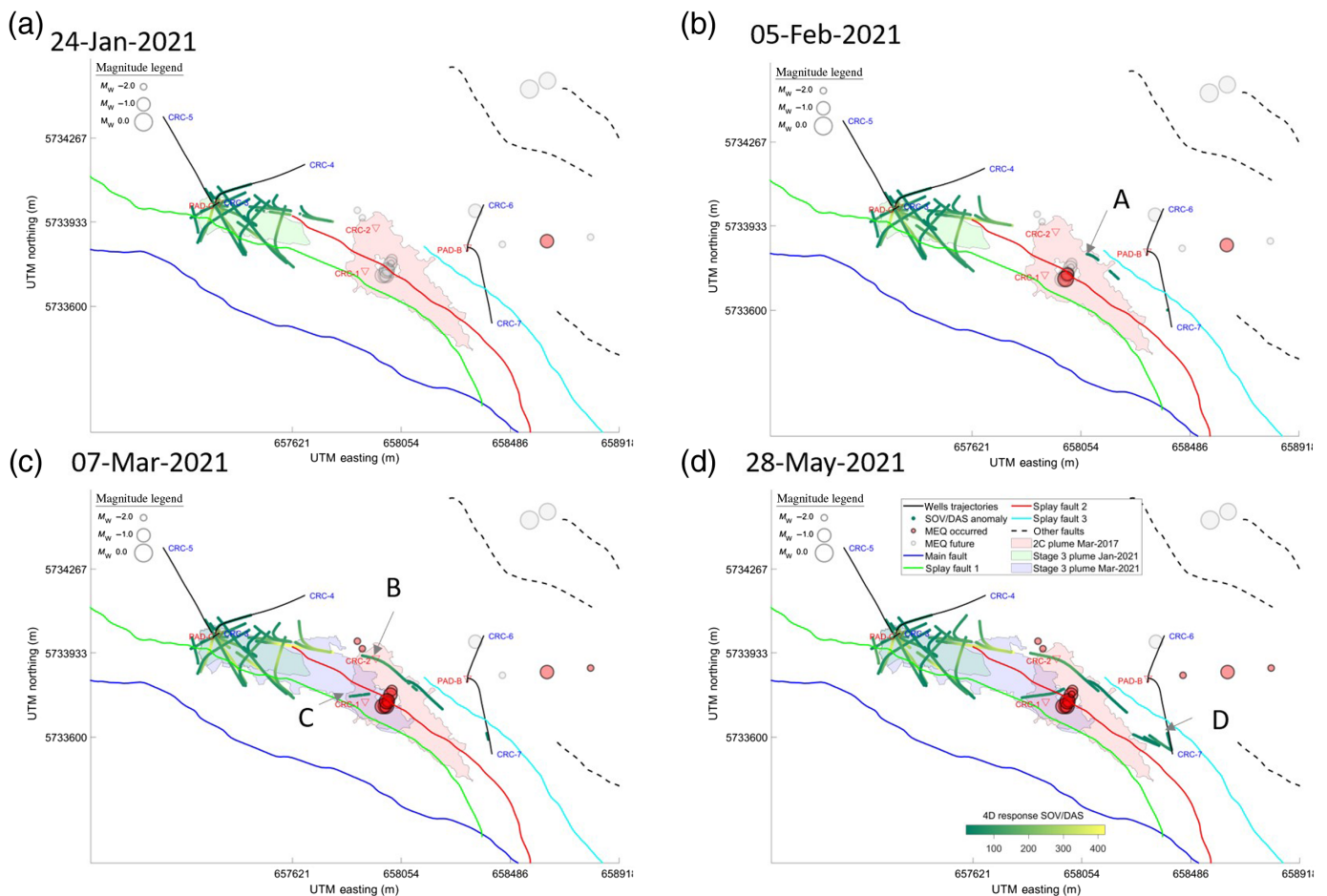


Figure 10. Relationship between the induced seismicity and movement of the injected supercritical CO₂ imaged by the continuous time-lapse VSP. (a) After 50 days, the injected CO₂ plume did not reach the Stage 2C plume, and only one event occurred close to the well pad B. (b) After 10 days, offset VSP anomalies indicated that the Stage 3 augmented the Stage 2C plume, which led to detectable seismicity within the Stage 2C plume. (c) After 90 days, the plumes merged according to both 3D and offset VSP, which led to more events triggered within the Stage 2C plume. (d) Finally, a few more events were triggered outside of the plumes. The color version of this figure is available only in the electronic edition.

References

- Alkhalifah, T., and I. Tsvankin (1995). Velocity analysis for transversely isotropic media, *Geophysics* **60**, no. 5, 1550–1566, doi: [10.1190/1.1443888](https://doi.org/10.1190/1.1443888).
- Beyreuther, M., R. Barsch, L. Krischer, T. Megies, Y. Behr, and J. Wassermann (2010). ObsPy: A python toolbox for seismology, *Seismol. Res. Lett.* **81**, no. 3, 530–533, doi: [10.1785/gssrl.81.3.530](https://doi.org/10.1785/gssrl.81.3.530).
- Brune, J. N. (1970). Tectonic stress and the spectra of seismic shear waves from earthquakes, *J. Geophys. Res.* **75**, no. 26, doi: [10.1029/JB075i026p04997](https://doi.org/10.1029/JB075i026p04997).
- Chevron (2021). Gorgon project carbon dioxide injection, *Annual Operational Report to WA State Government, 1 January 2021-31 December 2021, Tech. Rep.*, Western Australian Department of Mines, Industry Regulation and Safety, available at <https://www.documentcloud.org/documents/23253996-chevron-gorgon-project-carbon-dioxide-injection-report-2021-redacted> (last accessed June 2023).
- Cook, P. (2014). *Geologically Storing Carbon: Learning From the Otway Project Experience*, Csiro Publishing, Clayton, Australia.
- Egorov, A., R. Pevzner, A. Bóna, S. Glubokovskikh, V. Puzyrev, K. Tertyshnikov, and B. Gurevich (2017). Time-lapse full waveform inversion of vertical seismic profile data: Workflow and application to the CO₂CRC Otway project, *Geophys. Res. Lett.* **44**, no. 14, 7211–7218, doi: [10.1002/2017GL074122](https://doi.org/10.1002/2017GL074122).
- Glubokovskikh, S., R. Pevzner, J. Gunning, T. Dance, V. Shulakova, D. Popik, S. Popik, M. Bagheri, and B. Gurevich (2019). How well can

- time-lapse seismic characterize a small CO₂ leakage into a saline aquifer: Co2crc Otway 2c experiment (Victoria, Australia), *Int. J. Greenhouse Gas Control* **92**, 102854, doi: [10.1016/j.ijggc.2019.102854](https://doi.org/10.1016/j.ijggc.2019.102854).
- Glubokovskikh, S., R. Pevzner, E. Sidenko, K. Tertyshnikov, B. Gurevich, S. Shatalin, A. Slunyaev, and E. Pelinovsky (2021). Downhole distributed acoustic sensing provides insights into the structure of short-period ocean-generated seismic wavefield, *J. Geophys. Res.* **126**, no. 12, e2020JB021463, doi: [10.1029/2020JB021463](https://doi.org/10.1029/2020JB021463).
- Glubokovskikh, S., E. Saygin, S. Shapiro, B. Gurevich, R. Isaenkov, D. Lumley, R. Nakata, J. Drew, and R. Pevzner (2022). A small CO₂ leakage may induce seismicity on a sub-seismic fault in a good-porosity clastic saline aquifer, *Geophys. Res. Lett.* **49**, no. 12, e2022GL098062, doi: [10.1029/2022GL098062](https://doi.org/10.1029/2022GL098062).

- Goertz-Allmann, B., D. Kühn, V. Oye, B. Bohloli, and E. Aker (2014). Combining microseismic and geomechanical observations to interpret storage integrity at the in salah ccs site, *Geophys. J. Int.* **198**, no. 1, 447–461, doi: [10.1093/gji/ggu010](https://doi.org/10.1093/gji/ggu010).
- Harvey, S., S. O'Brien, S. Minisini, S. Oates, and M. Braim (2021). Quest ccs facility: Microseismic system monitoring and observations, *Proc. of the 15th Greenhouse Gas Control Technologies Conference*, 15–18 March 2021, doi: [10.2139/ssrn.3817042](https://doi.org/10.2139/ssrn.3817042).
- International Energy Agency (IEA) (2022). Global energy review: Co2 emissions in 2021, available at <https://www.iea.org/reports/global-energy-review-co2-emissions-in-2021-2> (last accessed June 2023).
- Isaenkov, R., R. Pevzner, S. Glubokovskikh, S. Yavuz, P. Shashkin, A. Yurikov, K. Tertyshnikov, B. Gurevich, J. Correa, T. Wood, *et al.* (2022). Advanced time-lapse processing of continuous das vsp data for plume evolution monitoring: Stage 3 of the co2crc Otway project case study, *Int. J. Greenhouse Gas Control* **119**, 103716, doi: [10.1016/j.ijggc.2022.103716](https://doi.org/10.1016/j.ijggc.2022.103716).
- Isaenkov, R., R. Pevzner, S. Glubokovskikh, S. Yavuz, A. Yurikov, K. Tertyshnikov, B. Gurevich, J. Correa, T. Wood, B. Freifeld, *et al.* (2021). An automated system for continuous monitoring of co2 geosequestration using multi-well offset vsp with permanent seismic sources and receivers: Stage 3 of the co2crc Otway project, *Int. J. Greenhouse Gas Control* **108**, 103317, doi: [10.1016/j.ijggc.2021.103317](https://doi.org/10.1016/j.ijggc.2021.103317).
- Jackson, S., J. Gunning, J. Ennis-King, C. Jenkins, T. Dance, M. Bagheri, and P. Barraclough (2021). Baseline monitoring for time-lapse pressure tomography: Initial results from Otway stage 3, *Proc. of the 15th Greenhouse Gas Control Technologies Conference*, 15–18 March 2021, doi: [10.2139/ssrn.3820165](https://doi.org/10.2139/ssrn.3820165).
- Jenkins, C., S. Marshall, T. Dance, J. Ennis-King, S. Glubokovskikh, B. Gurevich, T. La Force, L. Paterson, R. Pevzner, E. Tenthorey, *et al.* (2017). Validating subsurface monitoring as an alternative option to surface M&V - The CO2CRC's Otway Stage 3 injection, *Energy Procedia* **114**, 3374–3384, doi: [10.1016/j.egypro.2017.03.1469](https://doi.org/10.1016/j.egypro.2017.03.1469).
- Lellouch, A., N. J. Lindsey, W. L. Ellsworth, and B. L. Biondi (2020). Comparison between distributed acoustic sensing and geophones: Downhole microseismic monitoring of the FORGE geothermal experiment, *Seismol. Res. Lett.* **91**, no. 6, 3256–3268, doi: [10.1785/0220200149](https://doi.org/10.1785/0220200149).
- Lindsey, N. J., H. Rademacher, and J. B. Ajo-Franklin (2020). On the broadband instrument response of fiber-optic DAS arrays, *J. Geophys. Res.* **125**, no. 2, e2019JB018145, doi: [10.1029/2019JB018145](https://doi.org/10.1029/2019JB018145).
- Luo, B., G. Jin, and F. Stanek (2021). Near-field strain in distributed acoustic sensing-based microseismic observation, *Geophysics* **86**, no. 5, P49–P60, doi: [10.1190/geo2021-0031.1](https://doi.org/10.1190/geo2021-0031.1).
- Paitz, P., P. Edme, D. Gräff, F. Walter, J. Doetsch, A. Chalari, C. Schmelzbach, and A. Fichtner (2020). Empirical investigations of the instrument response for distributed acoustic sensing (DAS) across 17 octaves, *Bull. Seismol. Soc. Am.* **111**, no. 1, 1–10, doi: [10.1785/0120200185](https://doi.org/10.1785/0120200185).
- Pevzner, R., S. Glubokovskikh, R. Isaenkov, P. Shashkin, K. Tertyshnikov, S. Yavuz, B. Gurevich, J. Correa, T. Wood, and B. Freifeld (2022). Monitoring subsurface changes by tracking direct-wave amplitudes and traveltimes in continuous distributed acoustic sensor vsp data, *Geophysics* **87**, no. 1, A1–A6, doi: [10.1190/geo2021-0404.1](https://doi.org/10.1190/geo2021-0404.1).
- Pevzner, R., B. Gurevich, A. Pirogova, K. Tertyshnikov, and S. Glubokovskikh (2020). Repeat well logging using earthquake wave amplitudes measured by distributed acoustic sensors, *The Leading Edge* **209**, no. 3, 1622–1628, doi: [10.1093/gji/ggx109](https://doi.org/10.1093/gji/ggx109).
- Pevzner, R., R. Isaenkov, S. Yavuz, A. Yurikov, K. Tertyshnikov, P. Shashkin, B. Gurevich, J. Correa, S. Glubokovskikh, and T. Wood, *et al.* (2021). Seismic monitoring of a small CO₂ injection using a multi-well DAS array: Operations and initial results of Stage 3 of the CO2CRC Otway project, *Int. J. Greenh. Gas Control* **110**, 103437, doi: [10.1016/j.ijggc.2021.103437](https://doi.org/10.1016/j.ijggc.2021.103437).
- Pevzner, R., M. Urosevic, K. Tertyshnikov, H. AlNasser, E. Caspari, J. Correa, T. Daley, T. Dance, B. Freifeld, S. Glubokovskikh, *et al.* (2020). Chapter 6.1—Active surface and borehole seismic monitoring of a small supercritical co2 injection into the subsurface: Experience from the co2crc Otway project, in *Active Geophysical Monitoring*, Second Ed., J. Kasahara, M. S. Zhdanov, and H. Mikada (Editors), Elsevier, Amsterdam, Netherlands, 497–522, doi: [10.1016/B978-0-08-102684-7.00024-8](https://doi.org/10.1016/B978-0-08-102684-7.00024-8).
- Pirogova, A., R. Pevzner, B. Gurevich, S. Glubokovskikh, and K. Tertyshnikov (2019). Multiwell study of seismic attenuation at the co2crc Otway project geosequestration site: Comparison of amplitude decay, centroid frequency shift and 1d waveform inversion methods, *Geophys. Prospect.* **67**, no. 7, doi: [10.1111/1365-2478.12796](https://doi.org/10.1111/1365-2478.12796).
- Popik, S., R. Pevzner, A. Bona, K. Tertyshnikov, S. Glubokovskikh, and B. Gurevich (2020). P-wave anisotropy parameters estimation from multi-well 3d vsp using das: Stage 3 of the co2crc Otway project, *Geophys. Prospect.* **2020**, no. 1, 1–5, doi: [10.3997/2214-4609.202070032](https://doi.org/10.3997/2214-4609.202070032).
- Rohmer, J., A. Plummakers, and F. Renard (2016). Mechano-chemical interactions in sedimentary rocks in the context of co2 storage: Weak acid, weak effects? *Earth Sci. Rev.* **157**, 86–110, doi: [10.1016/j.earscirev.2016.03.009](https://doi.org/10.1016/j.earscirev.2016.03.009).
- Rotherth, E., and S. A. Shapiro (2007). Statistics of fracture strength and fluid-induced microseismicity, *J. Geophys. Res.* **112**, no. B4, doi: [10.1029/2005JB003959](https://doi.org/10.1029/2005JB003959).
- Saraji, S., L. Goual, M. Piri, and H. Plancher (2013). Wettability of supercritical carbon dioxide/water/quartz systems: Simultaneous measurement of contact angle and interfacial tension at reservoir conditions, *Langmuir* **29**, no. 23, 6856–6866, doi: [10.1021/la3050863](https://doi.org/10.1021/la3050863).
- Sarmadivaleh, M., A. Z. Al-Yaseri, and S. Iglauer (2015). Influence of temperature and pressure on quartz-water-co2 contact angle and co2-water interfacial tension, *J. Colloid Interface Sci.* **441**, 59–64, doi: [10.1016/j.jcis.2014.11.010](https://doi.org/10.1016/j.jcis.2014.11.010).
- Shashkin, P., B. Gurevich, S. Yavuz, S. Glubokovskikh, and R. Pevzner (2022). Monitoring injected co2 using earthquake waves measured by downhole fibre-optic sensors: Co2crc Otway stage 3 case study, *Sensors* **22**, no. 20, doi: [10.3390/s22207863](https://doi.org/10.3390/s22207863).
- Shearer, P. M. (2019). Earthquakes and source theory, in *Introduction to Seismology*, Third Ed., Cambridge University Press, 237–298, doi: [10.1017/9781316877111.010](https://doi.org/10.1017/9781316877111.010).
- Staněk, F., G. Jin, and J. Simmons (2022). Fracture imaging using das-recorded microseismic events, *Front. Earth Sci.* **10**, doi: [10.3389/feart.2022.907749](https://doi.org/10.3389/feart.2022.907749).
- Vasco, D. W., A. Rucci, A. Ferretti, F. Novali, R. C. Bissell, P. S. Ringrose, A. S. Mathieson, and I. W. Wright (2010). Satellite-based

- measurements of surface deformation reveal fluid flow associated with the geological storage of carbon dioxide, *Geophys. Res. Lett.* **37**, no. 3, doi: [10.1029/2009GL041544](https://doi.org/10.1029/2009GL041544).
- Vilarrasa, V., J. Carrera, S. Olivella, J. Rutqvist, and L. Laloui (2019). Induced seismicity in geologic carbon storage, *Solid Earth* **10**, no. 3, 871–892, doi: [10.5194/se-10-871-2019](https://doi.org/10.5194/se-10-871-2019).
- Wessel, P., and W. H. F. Smith (2014). New, improved version of generic mapping tools released, *Eos* **79**, 579, doi: [10.1029/98EO00426](https://doi.org/10.1029/98EO00426).
- White, J. A., L. Chiaramonte, S. Ezzedine, W. Foxall, Y. Hao, A. Ramirez, and W. McNab (2014). Geomechanical behavior of the reservoir and caprock system at the in salah co2 storage project, *Proc. Natl. Acad. Sci. Unit. States Am.* **111**, no. 24, 8747–8752, doi: [10.1073/pnas.1316465111](https://doi.org/10.1073/pnas.1316465111).
- Williams-Stroud, S., R. Bauer, H. Leetaru, V. Oye, F. Stanek, S. Greenberg, and N. Langet (2020). Analysis of microseismicity and reactivated fault size to assess the potential for felt events by co2 injection in the Illinois Basin, *Bull. Seismol. Soc. Am.* **110**, no. 5, 2188–2204, doi: [10.1785/0120200112](https://doi.org/10.1785/0120200112).
- Withers, M., R. Aster, C. Young, J. Beiriger, M. Harris, S. Moore, and J. Trujillo (1998). A comparison of select trigger algorithms for automated global seismic phase and event detection, *Bull. Seismol. Soc. Am.* **88**, no. 1, 95–106, doi: [10.1785/BSSA0880010095](https://doi.org/10.1785/BSSA0880010095).
- Yurikov, A., K. Tertyshnikov, S. Yavuz, P. Shashkin, R. Isaenkov, E. Sidenko, S. Glubokovskikh, P. Barraclough, and R. Pevzner (2022). Seismic monitoring of co2 geosequestration using multi-well 4d das vsp: Stage 3 of the co2crc Otway project, *Int. J. Greenhouse Gas Control* **119**, 103726, doi: [10.1016/j.ijggc.2022.103726](https://doi.org/10.1016/j.ijggc.2022.103726).

Manuscript received 30 January 2023

Published online 5 July 2023